Suppression of axial combustion instability in solid rocket motors

D. R. Greatrix
Department of Aerospace Engineering, Ryerson University, Canada

Abstract

A numerical model for the prediction of undesirable axial combustion instability symptoms in solid-propellant rocket motors is utilized in the process of demonstrating various approaches for suppressing this instability behaviour. The unsteady interior one- or two-phase flow in the motor chamber, the oscillation of the surrounding structure of the propellant and motor casing, and the corresponding transient combustion process, are all incorporated within this comprehensive model. Example numerical results are presented for a cylindrical-grain motor having differing characteristics with respect to particle loading and grain geometry (fore and aft cross-sectional area changes), in illustrating the effectiveness of the particular suppression technique being applied.
Keywords: solid rocket motor, combustion instability, particles, geometry.

1 Introduction

Over the last fifty years or so, there has been a number of research efforts directed towards understanding the physical mechanisms, or at least the surrounding factors, behind the appearance of symptoms associated with nonlinear axial combustion instability in solid rocket motors (SRMs). The motivation for these studies was and is of course to bring this better understanding to bear in more precisely suppressing, if not eliminating, these symptoms. Research towards predicting instability symptoms in SRMs necessitates comprehensive numerical models for interior ballistic simulation under dynamic flow and combustion conditions. An effective model combines the effects of the unsteady flow, the transient combustion process, and the structural dynamics of the surrounding propellant/casing structure. In the present
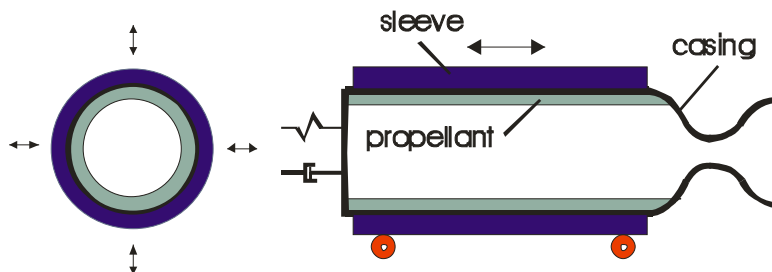
Figure 1:   SRM model setup.

investigation, a numerical model incorporating the above attributes is used in the prediction of the unsteady instability-related behaviour in a reference cylindrical-grain motor (sustained axial pressure wave presence, in this case), and various means for instability suppression are in turn demonstrated.

2   Method

A simplified schematic diagram of the physical system of an SRM placed on a static test stand is provided in fig. 1.   In this example, the cylindrical-grain motor is free to vibrate radially without any external constraint (i.e., only constrained as indicated by a thick steel static-test sleeve surrounding the aluminum flightweight casing), while axial motion is constrained to a large degree by the thrust-measuring load cell (represented here as a spring/damper) at the lefthand boundary.   Under nominal operating conditions, the internal gas flow moves smoothly from the burning propellant surface through and beyond the exhaust nozzle.

With respect to modelling the internal flow within the motor, a number of studies for SRMs having larger length-to-diameter (L/D) ratios have incorporated the use of a one-dimensional unsteady flow model, e.g., as done by Loncaric *et al* [1] and Greatrix [2,3] using a higher-order random-choice method (RCM) for the one- or two-phase flow solution. The effect of such factors as turbulence can be included through one or more additional equations that employ the information from the bulk flow properties arising from the one-dimensional equations of motion for the gas (and for the particles, if a two-phase flow solution).   In those cases where two- or three-dimensional flow effects can influence a particular aspect of the motor's interior ballistic behaviour, one might consider a multi-dimensional flow solution approach if a one-dimensional solution does not capture (or capture adequately) the phenomenon in question. For the purposes of the present study, a one-dimensional RCM approach will be utilized for the unsteady flow solution.

Structural vibration can play a significant role in nonsteady SRM interior ballistic behaviour, as evidenced by observed changes in combustion instability symptoms as allied to changes in the structure surrounding the internal flow (e.g., propellant grain configuration, wall thickness, material properties).   The

level of sophistication required for modelling the motor structure (propellant, casing, static-test sleeve, nozzle) and applicable boundary conditions (load cell on static test stand) can vary, depending on the particular application and motor design. Loncaric *et al* [1] employed a finite-element approach towards the structural modelling of a star-grain propellant configuration. In the present study, a cylindrical-grain configuration allows for a simpler approach from thick-wall theory, as reported by Greatrix and Harris [4]. The radial deformation dynamics of the propellant/casing/sleeve are modelled by a series of independent ring elements along the length of the motor. Axial motion along the length of the structure is modelled via beam theory, and bounded by the spring/damper load cell at the motor's head end. Viscous damping is applied in the radial and axial directions. Reference structural properties are assumed for an ammonium-perchlorate/hydroxyl-terminated polybutadiene (AP/HTPB) composite propellant surrounded by an aluminum casing and steel sleeve. For greater accuracy, some properties like the propellant/casing/sleeve assembly's natural radial frequency may be predetermined via a finite-element numerical solution, rather than via theoretical approximations.

The transient burning rate for the regression of the core periphery of the cylindrical propellant grain may be modelled through the Zeldovich-Novozhilov approach; see [5]. This phenomenological modelling technique applies an energy conservation criterion in coupling the heat conduction within the solid phase (the propellant) to the heat produced in the gas phase above the propellant surface. Conveniently, empirical or semi-empirical steady-state burning rate information may be used in place of more complex dynamic flame-based reaction rate equations. The principal equation for the nominal (or unconstrained) instantaneous burning rate r_b*, tying the solid phase to the gas phase, is given by:

$$r_b^* = r_{b,qs} - \frac{1}{(T_s - T_i - \Delta H_s / C_s)} \frac{\partial}{\partial t} \int_{-\infty}^{0} \Delta T dy \qquad (1)$$

where $r_{b,qs}$ is the quasi-steady burning rate (value for burning rate as estimated from steady-state information for a given set of local flow conditions), T_s is the burning surface temperature at the spatial position $y = 0$, Ti is the initial propellant temperature ($y < 0$ moving deeper into the propellant), and $\Delta T = T(y,t) - T_i$ is the temperature distribution within the propellant. The transient heat conduction in the solid phase can be solved by an appropriate finite-difference scheme. As reported by Greatrix [5], the actual instantaneous burning rate r_b may be found as a function of r_b* through the rate limiting equation:

$$\frac{dr_b}{dt} = K_b (r_b^* - r_b) \qquad (2)$$

The rate limiting coefficient K_b effectively damps the unconstrained burning rate r_b* when for a finite time increment Δt:

$$K_b < \frac{1}{\Delta t} \qquad (3)$$

The quasi-steady burning rate $r_{b,qs}$ can be found as a function of various parameters; in this study, as a function of local static pressure p, core flow velocity u (erosive burning component), and normal/lateral/longitudinal acceleration such that:

$$r_{b,qs} = r_p + r_u + r_a \qquad (4)$$

The equations needed for the coupled solution of $r_{b,qs}$ may be found in [1] and [3].

3 Results and discussion

The reference SRM for this investigation is a cylindrical-grain motor employing a nonaluminized AP/HTPB propellant, with characteristics, such as the solid propellant's specific heat C_s, as reported by Greatrix and Harris [4]; some parameters have been updated or added for the current effort. A thin steel sleeve of 4.7-mm thickness is in place for the reference static-test simulations. In fig. 2, one can view the general combustion response (here, in terms of nondimensional limit magnitude M_ℓ, defined by

$$M_\ell = \frac{r_{b,peak} - r_{b,o}}{r_{b,qs,peak} - r_{b,o}} , \qquad (5)$$

where unity would indicate a flat response) of the reference solid propellant, at differing values of the net surface heat release ΔH_s (sign convention: positive with exothermic output of heat). The propellant's resonant frequency f_r of approximately 1 kHz is established via the value set for K_b (20000 s^{-1}). The value of 1 kHz is consistent with regard to being within the range of observed values for composite propellants at typical base burning rates, and will allow for close to the worst-case scenario in being similar to the fundamental axial resonant pressure wave frequency f_{1L}. In an actual test firing for evaluation of an SRM's susceptibility to nonlinear axial combustion instability symptoms, after the initial travelling pulse disturbance is introduced into the flow of the motor chamber, an unstable motor will exhibit a sustained axial compression wave, on occasion accompanied by a substantial increase in the base chamber pressure (referred to as a dc shift). An initial pulsed-firing simulation run was completed as a starting reference for this study, in which no particles are present or any other suppression technique being applied. In fig. 3 for head-end pressure p_c as a function of time, one can see that at some point, the principal compression wave reaches its quasi-equilibrium strength from an initial disturbance pressure Δp_d of 2 atm, the sustained compression wave front arriving about every 1 ms,
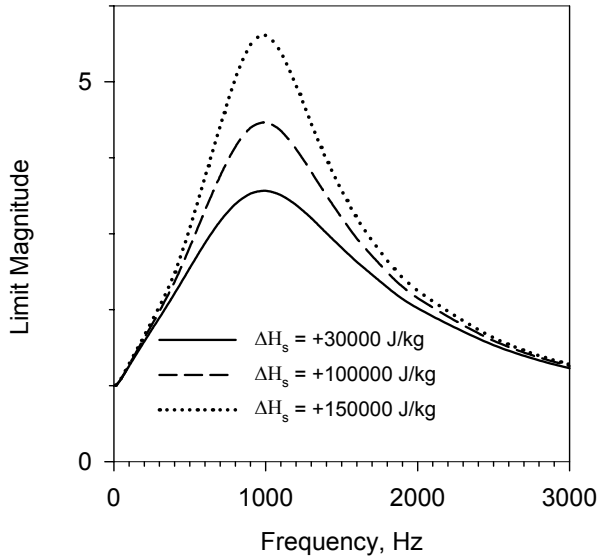
Figure 2:   Frequency response of ref. propellant (K_b = 20000 s^{-1}; differing values for ΔH_s; $r_{b,o}$ = 1.27 cm/s) in terms of nondimensional magnitude.

oscillating at the fundamental frequency f_{IL} of 1 kHz. The base pressure is not appreciably elevated over the nominal operating chamber pressure. The effect of normal acceleration on the burning process (related to the radial vibration of the motor propellant/casing; see [2,3]) has been nullified for this simulation (in order to isolate frequency-dependent Z-N combustion response as the predominant instability symptom driver for this and subsequent runs discussed in this paper), a factor in reducing the development of a dc shift. One can note that the limit pressure wave magnitude (Δp_w, peak-to-trough) is decreasing gradually with time after first reaching its quasi-equilibrium level, as the cylindrical grain burns back and the base pressure rises.

   One can refer to fig. 4 for the pressure-time profile for the same motor, but now with 5% particle loading (by mass) of inert spherical aluminium particles having a 12-μm diameter. Suppression of axial wave development after an initial 2-atm pulse is near-complete (limit magnitude of the sustained pressure wave, at 0.26 s, is about 0.042 MPa [Δp_w], as compared to 1.42 MPa for the 0% loading case noted earlier [$\Delta p_{w,peak}$], giving a nondimensional attenuation M_a, defined by

$$M_a = \frac{\Delta p_{w,peak} - \Delta p_w}{\Delta p_{w,peak}},\qquad(6)$$
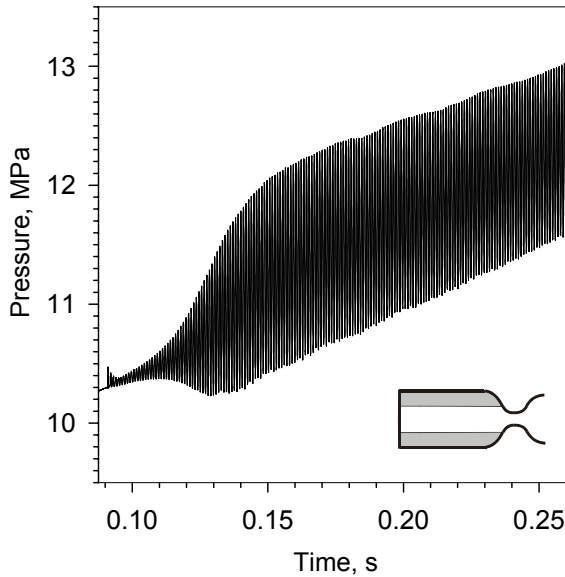
Figure 3: Predicted head-end pressure-time profile, reference motor (K_b = 20000 s^{-1}, ΔH_s = 150000 J/kg, Δp_d = 2 atm, α_p = 0%), acceleration nullified.

a value of 0.97, noting a value of unity is complete suppression). Historically, suppression of high-frequency tangential and radial pressure waves in SRMs by the use of particles in the range of 1 to 3% loading by mass has been in general largely successful. In the case of axial pressure waves, the effectiveness of particles from 1% to over 20% loading in suppressing wave development has been less consistent, relative to the previously mentioned transverse cases. In the case of fig. 4, remembering that acceleration as a factor has been nullified in the combustion process, a loading of 5% at 12 μm does appear to effectively suppress axial wave development in this particular motor, at this point in its firing.

An attenuation map for the above motor is provided in fig. 5. Here, various M_a curves are displayed as a function of aluminium particle diameter, with each curve being at a particular loading percentage. The case of fig. 4 is the approximate peak M_a point of the 5% loading curve in fig. 5. The x-axis in essence represents the 0% loading case (no suppression at any particle diameter). The same juncture in the firing simulations is the time reference for each point (0.26 s). Dobbins and Temkin [6], via acoustic (weak-wave) theory for low-Reynolds-number flow of a gas-particle mixture, reported the following well-known relation for the optimum particle diameter d_{opt} in attenuating pressure waves:

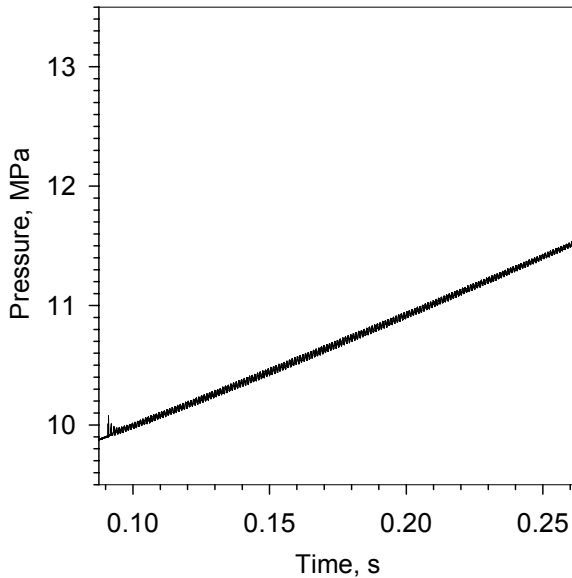$$d_{opt} = \sqrt{\frac{9\mu}{\pi f \rho_m}} \qquad (7)$$

Figure 4:   Predicted head-end pressure-time profile, reference motor (K_b = 20000 s^{-1}, ΔH_s = 150000 J/kg, Δp_d = 2 atm, α_p = 5%, d_m = 12 μm), acceleration nullified.

Here, μ is the gas absolute viscosity, ρ_m is the particle solid density, and f is the frequency of the oscillating axial pressure wave. For the present motor, eq. (7) would suggest a d_{opt} of around 9.2 μm, while fig. 5 suggests peak attenuation occurs at particle diameters of around 10 to 25 μm at very low loadings (around 1% for α_p, peak appears as a plateau range), narrowing and dropping somewhat towards 12 μm as one increases the loading from 1% towards 5%, and then again a spreading range (plateau peak) from that figure of 12μm at even higher loadings. It is not surprising that there would be a difference from the predicted acoustic-theory attenuation, given that the low-speed, weak-wave assumptions inherent in eq. (7) are not being presumed in generating the higher-flow-speed numerical results of fig. 5, specifically where both laminar- and turbulent-flow drag between the spherical particles and gas may in fact be present as a predominant attenuation/loss mechanism.

An alternative or complementary approach to the use of particles is to change the internal grain geometry to improve the suppression of observed symptoms. In practice, one sometimes notes that c.i. symptoms only occur within a certain timeframe within a given motor design's firing, suggesting that the grain shape during that interim period is somehow more susceptible to pressure-wave or dc shift development. Conversely then, outside of that time period, something about the grain's shape is acting to suppress symptom development. As an example, in fig. 6, one can see a comparison in limiting wave strength (measured
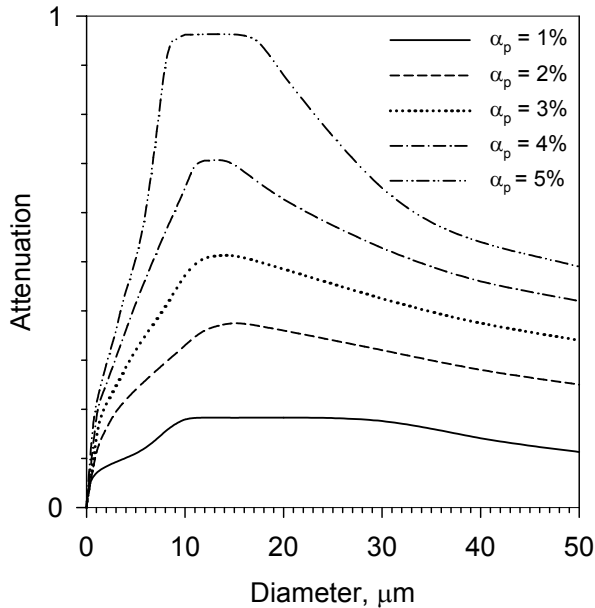
Figure 5: Nondimensional attenuation as function of particle diameter and loading, reference motor, acceleration nullified.

at the head end) at a later point in the firing with the introduction of a roughly 2:1 cross-sectional core area expansion (moving left to right) through the halfway point on the grain of the reference motor, reducing the pressure wave to about 25% of its reference strength. Note that the nozzle throat diameter was set at 1.7 cm (vs. the reference 1.6 cm) for the expansion case, for a comparable chamber pressure. Positioning the internal grain expansion at the one-quarter and three-quarter grain-length positions respectively was not nearly as effective.

Moving to the case of contracting the grain internal core cross-sectional area as one moves left to right, one can see from fig. 7 that at the one-quarter position, this technique is quite impressive in almost fully suppressing wave activity. The nozzle throat diameter was set at 1.68 cm (vs. the reference 1.6 cm) for the contraction case, for a comparable chamber pressure. Positioning the internal grain contraction at the halfway position is still very much effective in suppressing wave activity, while much less effective at the three-quarter position.

The analysis undertaken for this paper provides a few examples for how one might suppress, to some degree, instability symptoms within a given motor's design. By no means are these the only techniques available to the motor designer. Ramohalli [7] provides a good review of a number of techniques that have been attempted over the years.
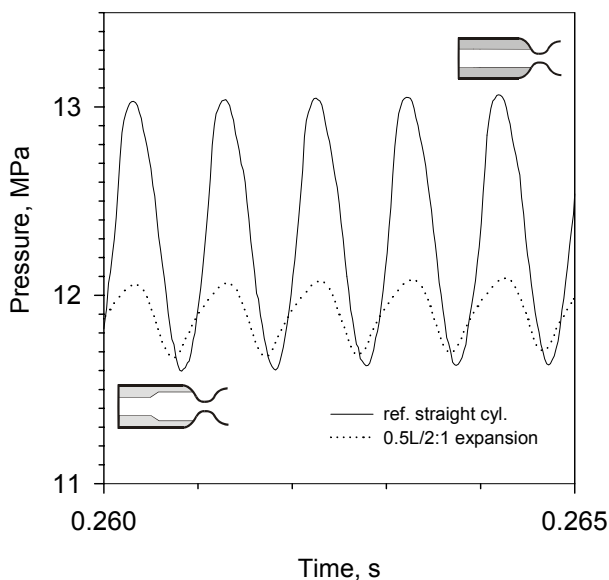
Figure 6: Predicted head-end pressure-time profiles, reference motor (K_b = 20000 s^{-1}, ΔH_s = 150000 J/kg, Δp_d = 2 atm, α_p = 0%), grain expansion case, acceleration nullified.
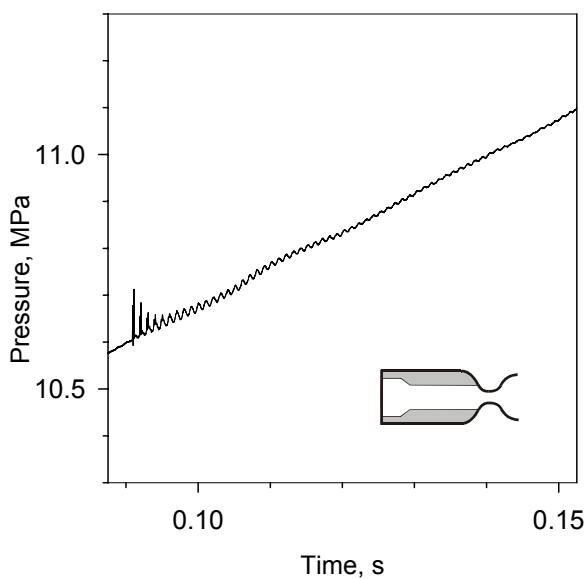

Figure 7: Predicted head-end pressure-time profiles, reference motor (K_b = 20000 s^{-1}, ΔH_s = 150000 J/kg, Δp_d = 2 atm, α_p = 0%), grain contraction case, acceleration nullified.

4   Concluding remarks

The implications of such factors as particle loading and grain geometry on nonlinear axial combustion instability symptom development and suppression have been demonstrated by the numerical simulation results presented in this study of a reference cylindrical-grain solid rocket motor. Unquestionably, further work remains to be done in establishing a more complete understanding of the various mechanisms involved in driving instability symptoms, so as to allow for more refined and targeted techniques in suppressing said symptoms.

References

[1]   Loncaric, S., Greatrix, D.R. and Fawaz, Z., Star-grain rocket motor — nonsteady internal ballistics. *Aerospace Science & Technology*, **8(2)**, pp. 47-55, 2004.

[2]   Greatrix, D.R., Nonsteady interior ballistics of cylindrical-grain solid rocket motors. Computational Ballistics II, WIT Press, pp. 281-289, 2005.

[3]   Greatrix, D.R., Predicted nonsteady internal ballistics of cylindrical-grain motor. AIAA Paper No. 2006-4427, 2006.

[4]   Greatrix, D.R. and Harris, P.G., Structural vibration considerations for solid rocket internal ballistics modeling. AIAA Paper No. 2000-3804, 2000.

[5]   Greatrix, D.R., Transient solid-propellant burning rate model: comparisons to experimental data. AIAA Paper No. 2006-4426, 2006.

[6]   Dobbins, R.A. and Temkin, S., Measurements of particulate acoustic attenuation, *AIAA Journal*, **2(6)**, pp. 1106-1111, 1964.

[7]   Ramohalli, K., Technologies and techniques for instability suppression in motors, *Nonsteady Burning and Combustion Stability of Solid Propellants*, edited by De Luca, L., Price, E.W. and Summerfield, M., Vol. 143, Progress in Astronautics & Aeronautics series, AIAA, Washington D.C., Ch. 20, 1992.